ADVANCED FUNCTIONAL MATERIALS
www.afm-journal.de

Triboelectricity Based Self-Powered Digital Displacement Sensor for Aircraft Flight Actuation

*Zhuyu Zhou, Zijie Xu, Leo N.Y. Cao, Hengrui Sheng, Chengyu Li, Yurui Shang, Wei Tang, and Zhong Lin Wang**

The utilization of unmanned aerial vehicles (UAVs) is on the rise across various industries. In such a scenario, the issue of flight safety for these UAVs becomes increasingly paramount. Currently, UAVs exhibit shortcomings in flight attitude perception compared to more mature manned aircraft, especially concerning the position sensing of flight actuation, which poses significant safety risks. Mature position monitoring solutions for flight actuation used in manned aircraft cannot be directly integrated into systems of UAV due to compatibility issues. This necessitates the development of new position sensing technologies to address this challenge. Triboelectric nanogenerators, with their advantages of miniaturization, self-powering capabilities, and the ability to generate voltage-level electrical signals, are chosen to form a part of the position detection system for sensors in UAVs. In this study, a self-powered displacement sensor is developed that utilizes frictional charge separation signals. This sensor is specifically designed to monitor the position status of the flight actuators in UAV. With a compact volume of <11.1 cm^3 and a weight of <9.5 g, this sensor is lightweight efficient and adaptable for practical applications.

1. Introduction

The development of aircraft is advancing at a rapid pace.[1] Manned aircraft have become an integral part of transportation,[2] while in recent years, the burgeoning field of unmanned aerial vehicle (UAV) has played a crucial supporting role in various professional sectors like film and television,[3] agriculture,[4] forestry,[5] power, and urban logistics.[6] To ensure flight safety and power efficiency,[7] various sensors are required to collect sufficient information about the status of UAVs.[8] For manned aircraft, a range of sensors,[9] such as angle of attack sensors,[10] airspeed indicators, stall sensors,[11] and sideslip angle sensors,[12] are already in place to ensure the safety of flight in various conditions. However, for UAV, apart from the most basic sensors like gyroscopes, accelerometers, and barometric pressure sensors,[13] there are no other sensors available to determine the aircraft's attitude (orientation including its pitch, roll, and yaw), posing a challenge to ensuring flight safety.[7b,14]

Position sensing of flight actuation is an important component of flight attitude control. The monitoring of flight actuation, especially the positions of wing control surfaces, is a fundamental sensing function, and its significance cannot be underestimated.[15] Modern manned aircraft typically incorporate corresponding position sensing systems for their actuators, such as position sensing systems for ailerons and flaps, and landing gear status sensing systems.[16] However, small UAV usually lack such position sensing systems for their actuators. The status of these actuators can only be determined based on experience of the operator, as there is no direct way to intuitively understand the movement, fault status,[17] and synchronization of actuator groups through sensor data.[18]

Furthermore, the integration of position monitoring systems used in manned aircraft onto UAV is often not feasible due to various reasons. Actuator position sensors employed in manned aircraft generally use mechanical, capacitive, inductive,[19] eddy current,[20] and optical signal technologies to sense the position status of the monitored components.[21] They convey specific status information to the operator through signal processing equipment at the back end. However, mechanical displacement sensors, while reliable and durable with strong interference

Z. Zhou
College of Engineering
Zhejiang Normal University
Zhejiang 321000, China

Z. Zhou, Z. Xu, L. N. Cao, H. Sheng, C. Li, Y. Shang, W. Tang, Z. L. Wang
CAS Center for Excellence in Nanoscience
Beijing Key Laboratory of Micro-nano Energy and Sensor
Beijing Institute of Nanoenergy and Nanosystems
Chinese Academy of Sciences
Beijing 101400, China
E-mail: zlwang@binn.cas.cn

Z. Xu, L. N. Cao, Z. L. Wang
School of Nanoscience and Technology
University of Chinese Academy of Sciences
Beijing 100049, China

H. Sheng, Y. Shang, W. Tang
Center on Nanoenergy Research
School of Physical Science and Technology
Guangxi University
Nanning 530004, China

Z. L. Wang
School of Materials Science and Engineering
Georgia Institute of Technology
Atlanta, GA 30332-0245, USA

DOI: 10.1002/adfm.202311839

resistance, are typically large and heavy. Inductive and eddy current displacement sensors, although capable of non-contact monitoring of actuator positions while maintaining a compact design, suffer from poor interference resistance and are limited in their application environments. Moreover, all the mentioned displacement sensors require active power for sensing signal, which can be an added burden on power management for UAVs. The challenge of weak position sensing capabilities in UAVs remains unresolved through existing sensor solutions.

Triboelectric nanogenerator (TENG) is an energy and sensing technology that has been gaining increasing attention in recent years, serving as units for generating signals through contact-induced charge separation.[22] Utilizing TENG technology allows for the development of self-powered, miniaturized sensors capable of functioning in diverse environmental conditions.[23] Moreover, owing to the high voltage characteristics of TENGs, even small sensors can generate voltage-level electrical signals, significantly enhancing the interference resistance of sensors produced using this technology.[24]

In light of this, we have developed a self-powered digital displacement sensor (SDDS) based on a grating structure with a free-standing layer of TENG. This sensor has been integrated into the wing of a UAV, allowing its stretching and contraction to synchronize with the movement of the UAV rudder surface or flaps. With a compact volume of less than 11.1 cm^3, a weight of less than 9.5 g, and excellent robustness, it can be used for the position monitoring of various flight actuators, including ailerons, flaps, vertical tail, and horizontal tail. Additionally, it can monitor the synchronization status of rudder groups and perform other extended functions. Through wind tunnel experiments and testing on multiple aircraft models, this research has demonstrated the feasibility and reliability of position monitoring sensing in various environments, offering the potential to be applied to practical flight actuation position monitoring.

2. Results and Discussion

2.1. . Device Structure and Working Principle

By combining badge reel structure and grating-structure TENG, we have developed a small SDDS for real-time monitoring of flight actuators of the aircraft. The device, as depicted in the exploded view in **Figure 1**a, comprises a lid, rotor, and stator assembled coaxially. The rotor consists of a clockwork spring, a badge reel spindle, and a freestanding layer of upper electrodes. On the other hand, the stator includes a dielectric material and grating electrodes that complement the upper electrode. The dielectric material used is fluorinated ethylene propylene (FEP). The grating electrodes on both the rotor and stator, combined with the FEP film attached to the stator electrodes, create a freestanding triboelectric-layer-based nanogenerator with a sliding frictional structure. The displacement of the rotor and stator is facilitated by the stretching and shrinking of the rope, which acts as the active side of the sensor. In practical application, the sensor is affixed to the wing or fuselage of the aircraft, and the rope is connected to the actuator to be monitored. When the monitored object moves, the sensor generates a corresponding electrical signal. The accuracy of the SDDS primarily depends on the grating spacing of electrodes on the rotor and stator (described as the angle between electrodes in the following) and the inner diameter of the badge reel spindle. The precise dimensions of the spindle and the two electrodes can be found in Figure S1 (Supporting Information).

A physical top view of the internal structure of SDDS, created using stereolithography (SLA) 3D printing technology with white photosensitive resin material, is presented in Figure 1b. The rotation of the stator and rotor is controlled by a rope wrapped around the badge reel, while the rotor is reset by a spring fixed to the stator shaft. Multiple electrode variations with different spacing were tested, and the most accurate electrode configuration was selected for the SDDS. Details of the electrodes used can be seen in Figure S2 (Supporting Information). The overall dimensions of the device, as shown in Figure 1c, are 42 mm in diameter and 7.4 mm in thickness. The compact size, lightweight, and thinness of this product guarantee minimal disruption to the flight of fixed-wing UAVs. Additionally, it creates a vortex generator (VG)-like effect that effectively postpones airflow separation in the boundary layer.

The process of electrical signal generation in the SDDS, which is based on the freestanding TENG, is illustrated in Figure 1d. As the rotor rotates, the copper freestanding layer rubs against the FEP dielectric layer, resulting in the generation of charges. The charge density on the rotor electrode is greater than that on the FEP film due to the charge transfer law of electrification by friction. Initially, the stator and rotor electrodes are aligned, and the positive charge carried on the rotor electrode induces a negative charge to accumulate on electrode A, while simultaneously driving the accumulation of an equal amount of positive charge with opposite polarity on electrode B. While the rotor slides, free electrons flow continuously from electrode A to electrode B through the external circuit. The freestanding layers drive the flow of free electrons, ensuring that the system remains in electrostatic equilibrium due to the electrostatic force.

However, in badge reel structures, a single freestanding layer pattern can only calculate the total distance of stretching and shrinking displacement without distinguishing the specific direction. To address this, we designed an electrode arrangement, depicted in Figure 1e, consisting of one set of rotor electrodes and three sets of independent and sequentially arranged stator electrodes. Three independent electrical signals with a fixed difference in phase are combined by simple data processing to produce a vector signal with directional discrimination. As can be seen in Figure 1d,e, one rotor electrode and six stator electrodes (three pairs of stator electrodes that are relatively independent on the circuit) are included in one electrode group. In an electrode group, since there is only one rotor electrode, only one pair of stator electrodes works at the same time. With such an electrode design, a vector signal that can indicate the direction of rotor electron motion can be obtained by using a multi-channel signal acquisition device to acquire the electrical signals output from the three pairs of electrodes and combining the three signals through a back-end system. As shown in Figure 1e, when the rotor electrodes move to the right, the output signals are sorted from signal A to C. When the rotor electrodes move to the left, the signals sorted from C to A are obtained, and the two differently arranged signals indicate the direction of rotation of the rotor. Furthermore, Figure 1f presents the results of finite element analysis on the open circuit potential distribution for a set of electrodes during sliding in the freestanding layer mode, clearly

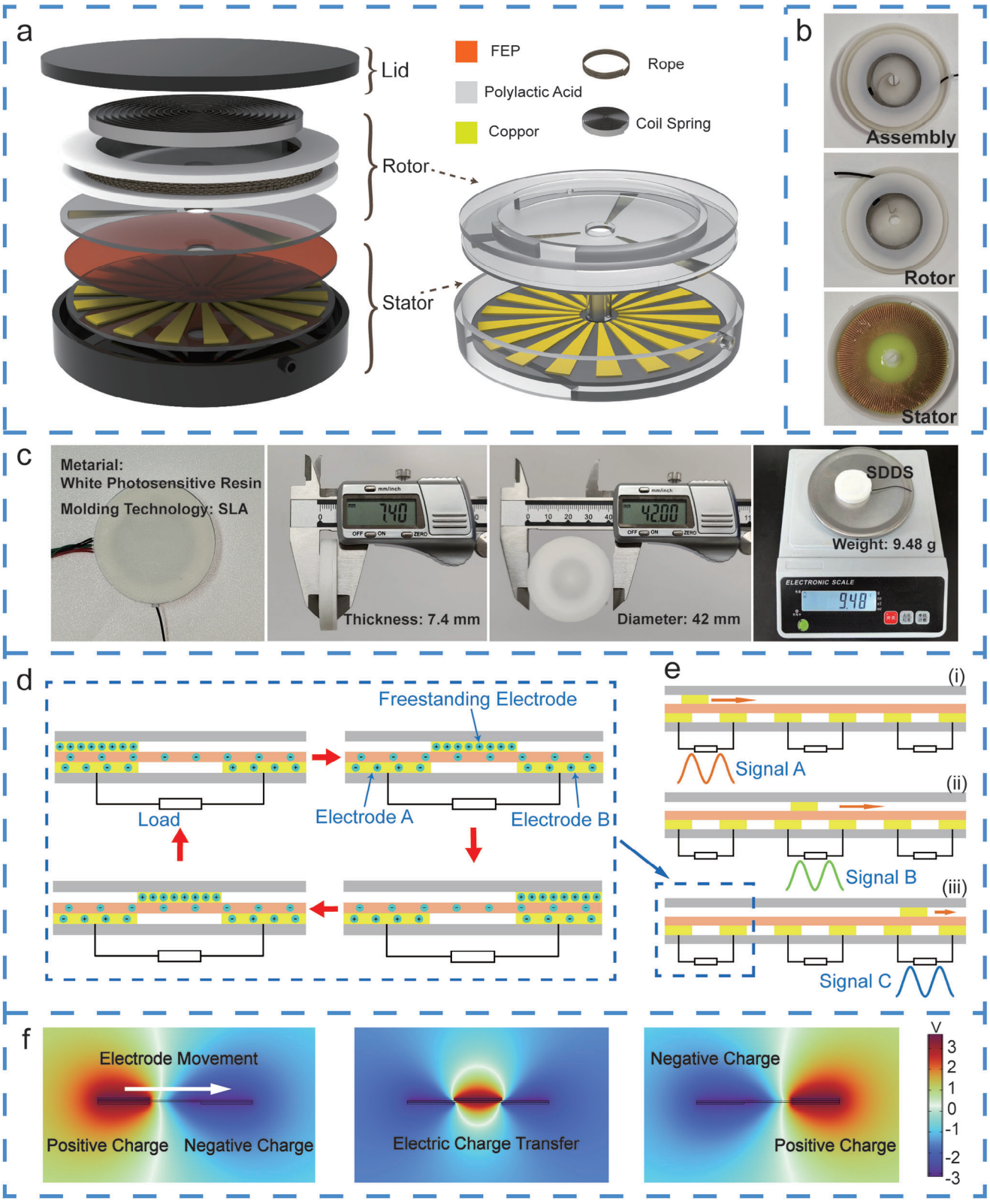

Figure 1. Structure, electrode arrangement, and analog simulation of SDDS. a) Exploded view of the SDDS, consisting of lid, rotor, and stator. b) Photographs of the rotor and stator and their assemblies. c) Photograph of the SDDS after packaging and its thickness, diameter, and weight. d) Charge-transfer processes in freestanding TENG. e) Design of electrode arrangement for vector displacement sensing. f) Finite element analysis of the potential distribution of a freestanding TENG.

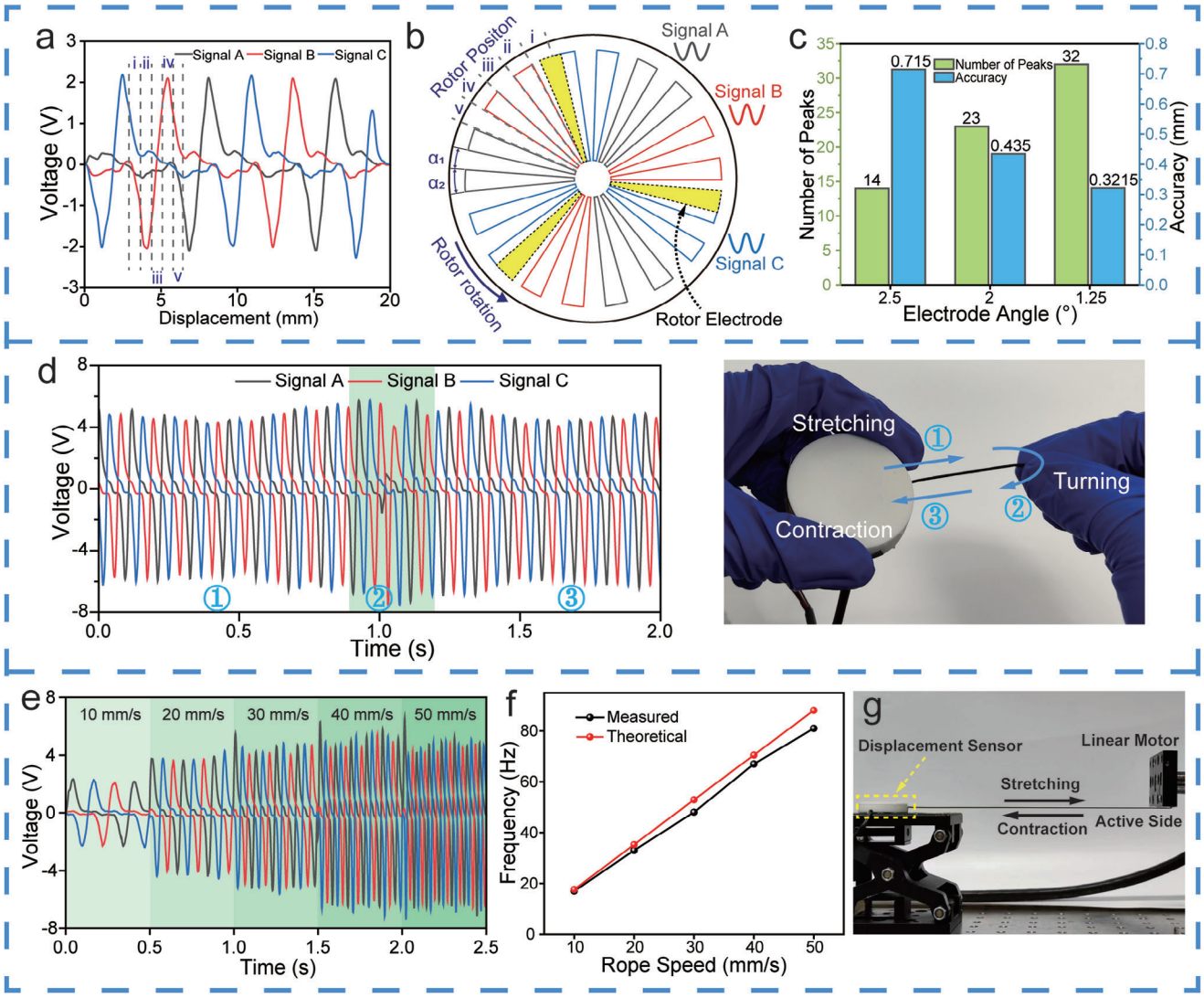

Figure 2. Signal generation and displacement calculation for SDDS. a) The voltage signal output from the SDDS consists of three sets of voltage signals with a fixed phase difference. b) Electrode distribution on the stator electrode. c) Number of peak electrical signals and accuracy of SDDS with different electrode angles at 20 mm. d) Stretch, contraction and turn signals. e) Electrical signals of SDDS at different speeds. f) Relationship between the frequency of peak sensor signals and the speed of stretching. g) Activity side of SDDS stretch and shrink under the control of linear motors.

demonstrating the field distribution and variation of the voltage during sliding.

2.2. Signal Analysis

The triboelectric charge separation signal of the device is output from three sets of independent freestanding layer electrodes. These signals are integrated and represented as three sets of electrical signals with a phase difference, as illustrated in **Figure 2**a. The electrical signals are acquired using a multi-channel signal acquisition system and processed accordingly. In a complete voltage waveform, which encompasses the entire voltage signal from negative to positive, the relative position of the rotor electrode with respect to the stator electrode can be more clearly identified. The complete electrical signal can be decomposed into five processes, as depicted in Figure 2a (signal part) and Figure 2b (relative position of the rotor electrode and the stator electrode, the rotor electrodes are labeled in yellow parts in the figure): a) The rotor electrode is located between the last set of stator electrodes and the next set of stator electrodes (position i), and the negative voltage gradually increases. b) The rotor electrode completely covers electrode A, and the negative voltage reaches its peak (position ii). c) The rotor electrode moves between electrode A and electrode B, and the voltage direction turns from negative to positive (position iii). d) The rotor electrode overlaps with electrode B, and the positive voltage reaches its peak (position iv). e) The positive electrical signal gradually decreases (position v). In Figure 2b we label the specific positions to which the rotor electrodes rotate (position i to position v as described above), and when the rotor electrodes move to these positions an electrical signal is generated as described in the process above. Meanwhile, $\alpha 1$ and $\alpha 2$

labeled in the figure denote the gap and electrode width of the stator electrodes, respectively ($\alpha 1 = \alpha 2$ in the test). And in the electrode arrangement of the rotating-disk TENG, we use the angle to denote the electrode width.

Due to electrostatic induction, the charge on the stator electrode receives induction from the rotor electrode and starts to flow even before the rotor electrode moves to position $\alpha 1$ (before it starts to cover the stator electrode). Hence, the next signal starts to be generated before the previous one has completely disappeared (in Figure 1a, signal A starts to be generated before signal C goes to zero). Additionally, since the freestanding layer electrodes are already induced with the next electrode as they exit the previous electrode, the induced signals begin to fluctuate significantly earlier than the point at which the previous signal is zeroed out. Furthermore, as a result of signal post-processing, when a high-frequency signal is generated during high-speed rotation, the inductive signal also reaches its peak earlier than the previous signal. This makes it difficult to determine the position of the rotor electrodes based solely on processes a–e) mentioned above.

Furthermore, we conducted accuracy performance measurements for the device at three different angles of electrodes, along with the number of signal peaks produced by a 20 mm stretch, as depicted in Figure 2c. The accuracy mentioned in the figure is calculated from Equation (1),

$$acc = \frac{\pi d}{2}\left(\frac{\alpha_1 + \alpha_2}{360^\circ}\right) \tag{1}$$

where acc is the accuracy, α_1 is the gap of two electrodes, and α_2 is the width of electrode, d is inner diameter of rotor which is displayed in Figure S1 (Supporting Information).

By measuring the number of peaks in a certain range, we can calculate the displacement of the object under test and the actual accuracy of the device, and from the figure we can get a minimum accuracy of 0.3215 mm for SDDS under ideal conditions. Notably, the device we tested utilized a spool with an inner diameter of 26 mm and a rope with a cross-sectional diameter of 0.8 mm. Taking into account the thickness of the rope became crucial as it influenced the measurements, causing them to fluctuate within a range. The accuracy of the device increased with fewer rope winding turns and longer stretching distances due to a decrease in the actual wire diameter. In Figure 2d, we observe the electrical signals during a stretch and contraction cycle, which can be divided into three parts. During stretching, the triboelectric signals appear in reverse order (labeled as A-B-C in positive order) and marked with ① (as shown in Figure 2d)in the signal diagram. When the stretching and contraction actions occur consecutively, a steering signal is generated (highlighted in blue and labeled as ② in the diagram). Finally, during contraction, the three signals are arranged in positive order. By analyzing the arrangement of the electrical signals, we can determine the exact position of the rotor electrodes relative to the stator electrodes based solely on the peaks of the signals. However, this approach sacrifices the motion details. For a thorough analysis of the signals in this aspect, please refer to Figure S3 (Supporting Information). Nevertheless, by monitoring the signal when the rotor changes direction of rotation using an electrostatic meter, we can precisely determine the position at which the rotor changes direction. Figure S4 (Supporting Information) provides a graph of the data for this particular section. Consequently, the direction of motion of the monitored object can be determined by the order of the signal arrangement. As illustrated in Figure 2e, we measured the voltage signal of the device at different motion speeds, using a linear motor to control the displacement speed (motor testing is shown in Figure 2g; Video S1, Supporting Information). As the speed increased, the frequency and voltage value of the generated electrical signal also rose. This correlation results from the increased displacement velocity and the frequency of charge exchange on the stator electrodes. With a fixed amount of transferred charge, the current increases with the rise in electrode velocity. We used a fixed-resistance signal acquisition system to measure the voltage, leading to an increase in voltage value with the rising current. Figure 2f presents the frequency of the generated signal peaks at different stretching speeds, depicting a linear increase in the frequency of the electrical signal output with various stretching speeds. The calculation of the theoretical values in Figure 2f is given by Equation (2),

$$f = \frac{v}{\pi d\left(\frac{\alpha_1+\alpha_2}{360^\circ}\right)} \tag{2}$$

where f is the frequency of output signal, v is stretching and contracting speed of rope, α_1 is the gap of two electrodes and α_2 is the width of electrode, d is inner diameter of rotor.

2.3. Signal Testing in Different Environments and Situation

We conducted tests to evaluate the performance of the displacement sensor in different environments. **Figure 3**a shows the voltage signal output of the sensor at different temperatures. The signal remained stable until 50 °C, with voltage levels ≈ 6 and 7 V at room temperature. However, the voltage signal dropped significantly at temperatures between 60 °C and 70 °C, with average voltages of only 3.15 and 2.5 V. Figure 3b displays the electrical signal waveforms of the displacement sensor at temperatures of 10 °C and 70 °C. Despite the lower signal strength at higher temperatures, the peak of the signal can still be distinguished, enabling accurate displacement sensing. Additionally, we tested the signal output performance of the sensor under different humidity levels, as depicted in Figure 3c. The electrical signal remained stable at different humidity levels, consistently above 6.5 V, indicating that the sensor functions properly in high humidity environments. Furthermore, we compared the signal performance of the sensor at the relative humidity (RH) of 16% and 90% in Figure 3d. While the signal strength decreased at RH of 90%, the displacement signal remained clear, indicating minimal impact on the sensing function. It should be noted that previous studies have shown that humidity can significantly affect the triboelectric charge separation signal, suggesting the need for better moisture barrier when using the sensor in such environments.

To assess the durability of the device, we subjected it to 180 000 cycles of pulling using a linear motor. The voltage signal variation during the test is depicted in Figure 3e. Initially, the signal increased and reached saturation due to charge accumulation on the surface of the freestanding and dielectric layers. However, as time goes by, the signal decreased due to

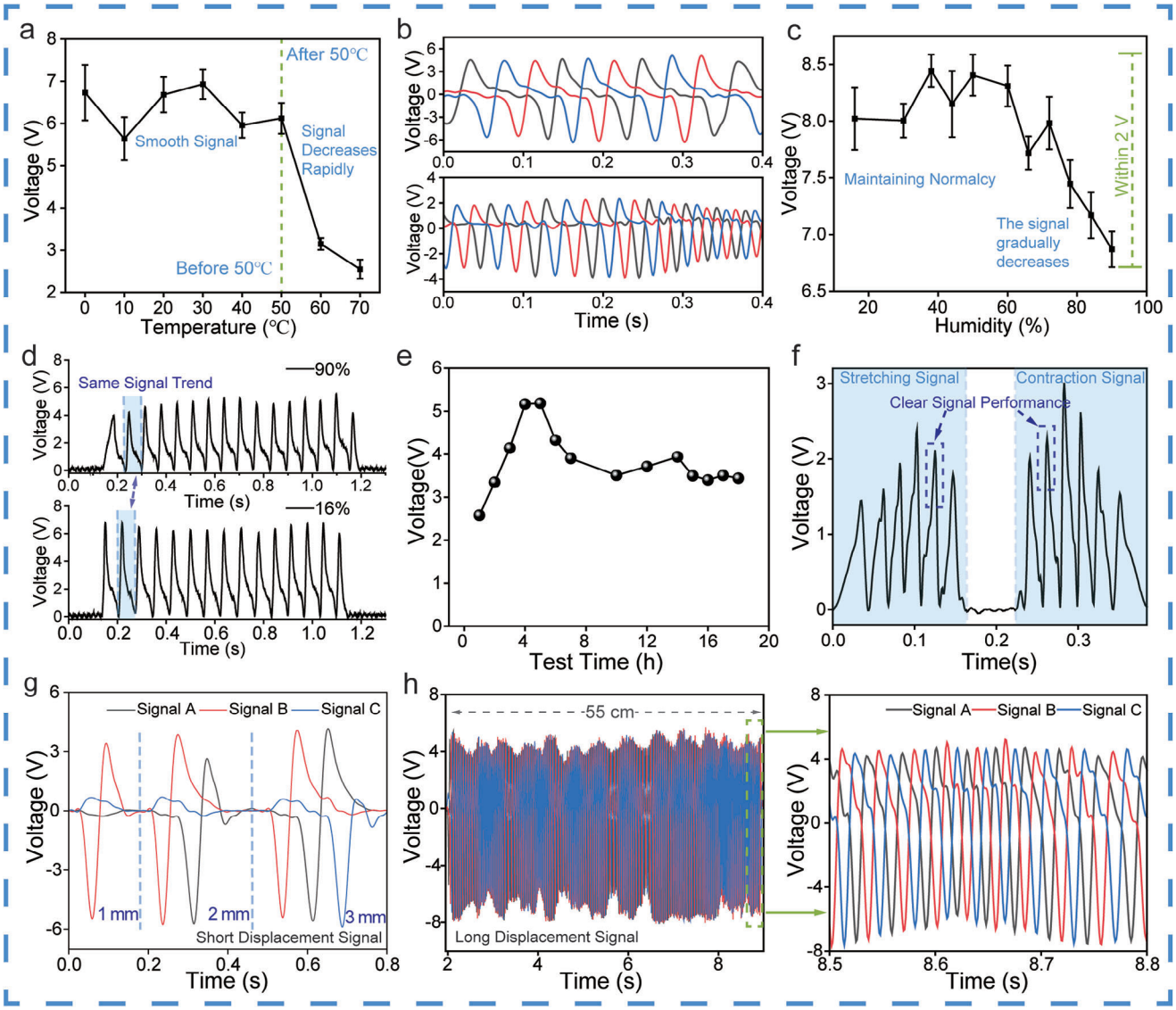

Figure 3. Signal performance of SDDS in different environments. a) Signal output of SDDS at different temperatures. b) Output signals at 10 °C (top) and 70 °C (bottom). c) Signal output at different humidity levels. d) Signal output of SDDS at RH of 90% and 16%. e) Durability test of the sensor with a stretch distance of 4 cm and a frequency of 2.5 Hz. f) Signal output after 20 h of stretching. g) Signal performance at stretch distances of 1, 2, and 3 mm. h) Signal output at 55 cm stretch and corresponding signal details.

wear on the dielectric layer. After 18 h, the output rapidly decreased until the average voltage dropped about 2 V. Figure 3f demonstrates the output signal of the device after 20 h of continuous operation, where the displacement signal was still discernible despite lower electrical output. These tests demonstrated the device's robustness in terms of temperature, humidity, and endurance.

In Figure 3g,h, we assessed the sensor's performance in measuring short and long displacements. For short displacements of 1, 2, and 3 mm, the sensor successfully monitored the displacement, as displayed in the electrical signals. In the long displacement test, we used a spool with more rope turns to move the object 55 cm, and the actual displacement distance could be calculated by observing the output signal.

2.4. Applications in Aircraft

By combining with UAV flight control and navigation systems, we have developed a real-time position feedback system for flight actuators of small UAVs. The workflow of the system is demonstrated in **Figure 4**a. When the flight actuator is active, it drives the movement of the active end of the SDDS, generating a friction separation charge signal to the multi-channel signal acquisition system, which passes the signal through the charge amplifier and digital-to-analog conversion module to the microcontrol unit via the serial peripheral interface (SPI). The microcontrol unit processes the signal and then passes it to the wireless module via the universal asynchronous receiver/transmitter (UART), and transmits the signal to the ground station or smart terminal, whose data processing system will process the

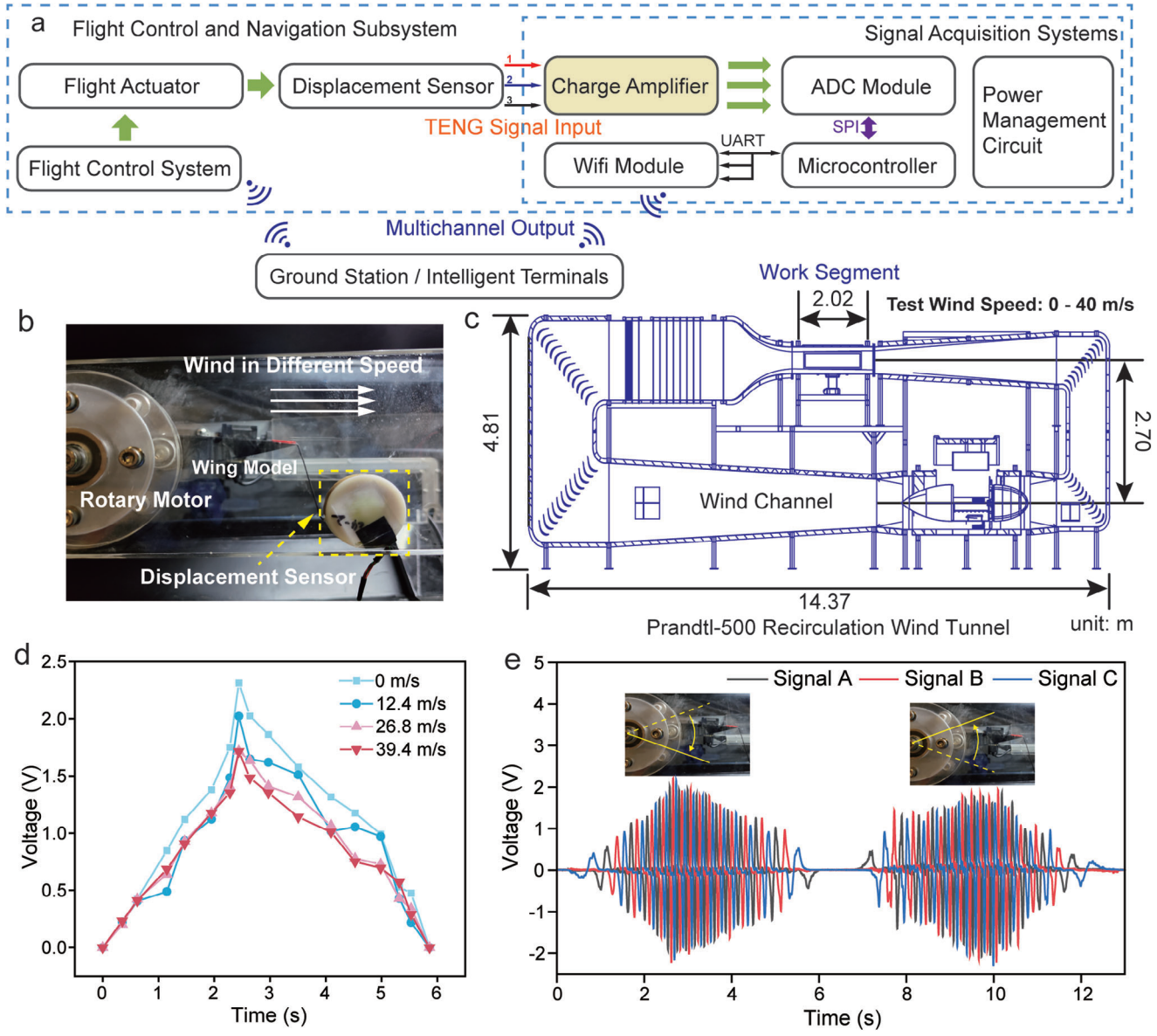

Figure 4. Wind tunnel testing of SDDS. a) Flowchart of a real-time aircraft actuator position status monitoring system. b) SDDS tested at different wind speeds, wing take-off and landing controlled by a rotary motor connected to the wing model. c) Structural diagram of the wind tunnel used for the tests (Prandtl-500 recirculation wind tunnel). d) Output curves at different wind speeds. e) The output signal of the sensor when testing the displacement of the wing model, wind speed is 0 m s^{-1}.

signal data into actuator position status information for forwarding to the flight control system and the controller. This feedback system will alert the controller when an abnormal signal is present.

To evaluate the performance of the sensor in high wind speeds, we conducted tests in a wind tunnel (Figure 4b), using the Prandtl-500 recirculation wind tunnel as shown in Figure 4c. The sensor was mounted on a model wing with a motor-controlled angle of attack, and its signal output was measured at wind speeds ranging from 0 to 39.4 m s^{-1}. The specific output signals of the SDDS for each wind speed are presented in Figure S5 (Supporting Information). As illustrated in Figure 4d, the sensor's output signal is minimally affected by the wind speed, with fluctuations within 1 V. With the takeoff and landing signals of the wing model (Figure 4e), we can also obtain more information about the motion state of the device under test based on the frequency and magnitude of the electrical signal generation.

We further tested the SDDS on a Cessna 182 model (**Figure 5**a). Figure 5b demonstrates the signal acquisition system and the SDDS that we used. The multi-channel signal acquisition system allowed us to simultaneously collect the position information of the aileron group or the flap group. Monitoring the aileron position required placing the sensor close to the main wing tip, where it acted as a partial winglet, reducing wingtip vortex strength and drag. Signals were tested separately for aileron motion above

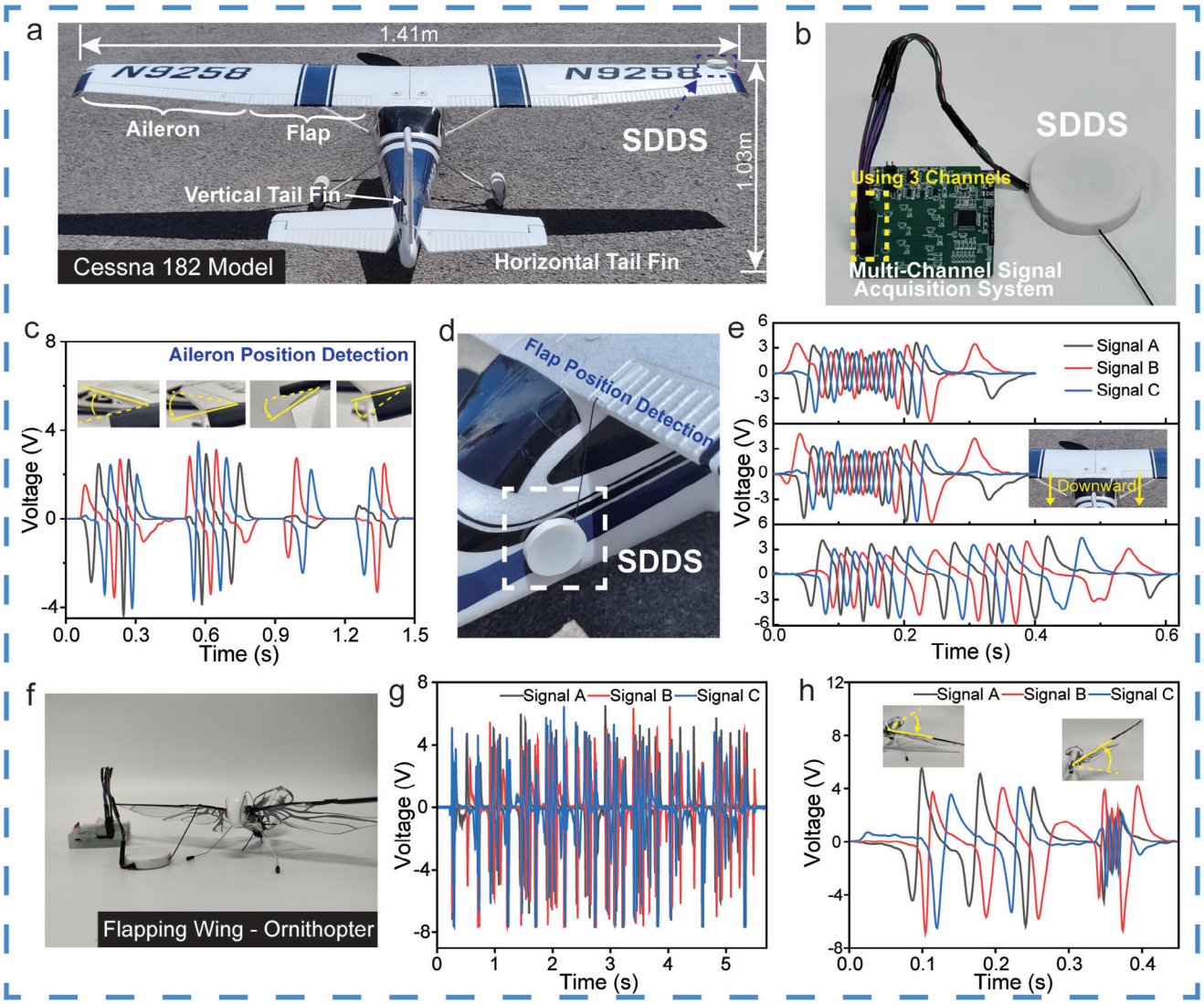

Figure 5. Position monitoring of vehicle actuators. a) Cessna 182 model for testing. b) Photograph of multi-channel signal acquisition system and SDDS. c) Electrical signals from SDDS when measuring the ailerons of fixed-wing aircraft. d) Sensors are mounted on the fuselage to monitor the position of the flaps. e) Synchronization signals (first two) and abnormal signals (third) generated during flap activity. f) A flapping wing aircraft for testing. g) Signal output when monitoring flapping. h) Electrical signals from a fluttering wing during a flutter.

and below the main airfoil (Figure 5c). Specific aileron test is demonstrated in Video S2 (Supporting Information). Due to limitations in the sensor structure, signals obtained for aileron position above the main airfoil had a significantly higher number and frequency compared to those for aileron position below the main airfoil, indicating different accuracy levels when monitoring aileron position.

For monitoring the position of the flaps, the installation shown in Figure 5d was employed. Flaps are crucial for landing and takeoff control in fixed-wing aircraft. Under normal operation, the positions of both flaps are synchronized, and monitoring them simultaneously using a displacement sensor generates an approximate displacement signal (shown in the first two sets of signals in Figure 5e). However, when one of the flaps moves abnormally, such as failing to move or moving out of sync, a distinct displacement signal is generated (third signal in Figure 5e). This allows us to identify faulty flaps and transmit the fault signal to the ground station via the wireless module, triggering an alarm.

Finally, the SDDS was used to monitor the real-time status of the actuator of an ornithopter (Figure 5f). The active end of the displacement sensing was connected to the wings of the ornithopter to capture the displacement signal as the wings flap up and down (Figure 5g). By analyzing the displacement signals, we can differentiate the motion speed by the difference in signal frequency generated during upward and downward wing motion. When both flaps are connected simultaneously, the system can also serve as a synchronization monitor similar to flap monitoring. However, as Figure 5f illustrates, our sensing system is currently too heavy and too large for direct application in such a scenario when compared to a micro-ornithopter.

3. Conclusion

In this work, we have developed a self-powered displacement sensing system based on freestanding TENGs. We have conducted rigorous tests to evaluate the sensor's performance in challenging environments such as high temperature, high humidity, and high wind speed conditions. The results have demonstrated that the SDDS exhibits robustness, environmental adaptability, and durability. Moreover, we have successfully developed a real-time displacement sensing monitoring system using the SDDS. This system allows for the monitoring of the motion of the device under test, and we have applied it effectively in the position monitoring of aircraft actuators. This demonstrates the feasibility of using the SDDS in practical flight applications, broadening the range of sensors available for small aircraft and ensuring a certain level of flight safety. However, there are certain issues that need to be addressed. The sensor's accuracy experiences some fluctuations due to its structure, and these fluctuations are more pronounced when monitoring aileron position. Additionally, the sensing function of the device may be compromised in prolonged high humidity environments, as this can affect the performance of TENG. In future research, we aim to overcome these challenges through structural optimization and material studies to enhance the sensor's accuracy and reliability.

4. Experimental Section

SDDS System Integration: The SDDS system consisted of three parts: TENG electrodes and triboelectric-layers, rotating mechanical structure, and data processing system. TENG electrode pairs were made using a printed circuit board (PCB) prototyping process using a 0.6 mm thick FR-4 Epoxy Glass Cloth substrate and an electrode thickness of 1 oz (oz is the common industrial usage and was ≈35 µm). On this basis the soldermask layer covering the electrodes had also removed so that the electrodes were exposed and could came into direct contact with the triboelectric-layer or act directly as triboelectric-layer. The precision and durability of TENG electrodes was maximized using proven industrial production techniques. We also tried the thinner flexible material polyimide for the base material, but its cost and durability disadvantages led us to choose FR-4 Epoxy Glass Cloth after all considerations. The copper electrode were used directly on the rotor as the positive triboelectric material and chose FEP as the negative triboelectric material, which was determined by the starting electrical properties of both copper and FEP.

For the implementation of the mechanical structure, white resin was used, polylactic acid (PLA) and high strength grey nylon. The grey nylon was highly resistant to temperature and high strength, making it suitable for use in harsh environments, but its own rough surface increased the friction of the part during rotation, while in high temperature tests, PLA showed deformation at over 60 °C. Based on these results, we finally chose white resin as the structural base material. The TENG electrodes were glued to the top of the bottom housing (as the stator) and the bottom of the rotor (as the rotor) using 502 glues, and a FEP film (0.025 mm) was applied to the surface of the stator to form a separate layer of TENG. A thin wire (0.8 mm nylon wire) was fixed to the side of the rotor for pulling the rotor and a volute spring (clockwork spring) was connected in the middle of the rotor to the central shaft of the bottom housing for resetting the rotor. With these steps, the SDDS system was basically assembled.

Data Collection of Real-Time Position Feedback System: In this work, signal acquisition and transmission were achieved by a multi-channel wireless signal acquisition system consisting of a charge amplifier, an 8-channel A/D converter chip, an STM-32 master control chip, a WIFI chip, and a power management module. After the charge amplifier acquired and regulated the friction charge signal, it converted the analogue voltage signal into a digital signal via the digital-to-analogue converter module, transferred the data to the STM-32 for processing via the SPI and passed it to the WiFi module by using UART, which transmitted the data to a smart terminal (in this experiment, the using a mobile personal computer as the terminal) to enable real-time monitoring.

Characterizations: The triboelectric signal in this work was measured by Keithley 6517 electrometer, and the wireless electrical signal was collected by STM-32 low-power microcontroller with a self-developed associated program. The grating electrodes were designed with Altium Designer software and produced by PCB prototyping technology (Rongxin Electronic Technology Development (Shenzhen) Co., Ltd.). 3D model design via Soildworks 2020 software. Resin 3D printing service by Nanjing Yue Shang Network Technology Co., Ltd. FEP film provided by Shanghai Witteland Industrial Co., Ltd. The dimensions of the spring used are 0.16 mm (thickness) × 2 mm (width) × 330 mm (length) (Shenzhen Dongji Intersprings Co., Ltd.). The linear motor used was LinMot E1100 (Kerry Linmot (Suzhou) Co., Ltd.). The wind tunnel tests in this work used Prandtl-500 recirculation wind tunnel (Tianjin Prandtl Co., Ltd.). The airfoil segment in the wind tunnel was obtained using CNC machining and was made of stainless steel, the wing was controlled by stepper motors (Cangzhou Kederuier Experimental Equipment Co., Ltd.). Cessna 182 model aircraft with 1.4 m fixed-wing was purchased from Yigou Aviation Technology.

Supporting Information

Supporting Information is available from the Wiley Online Library or from the author.

Acknowledgements

Z.Z., Z.X., and L.N.Y.C contributed equally to this work. The research was supported by the National Key R&D Project from the Minister of Science and Technology (2021YFA1201601); National Natural Science Foundation of China (Grant Nos. 51432005, 51561145021, and 52203324); the Fundamental Research Funds for the Central Universities (E2E46804).

Conflict of Interest

The authors declare no conflict of interest.

Data Availability Statement

The data that support the findings of this study are available from the corresponding author upon reasonable request.

Keywords

aircraft monitoring, digital sensors, displacement sensors, self-powered, triboelectric nanogenerators

Received: September 27, 2023
Revised: October 23, 2023
Published online:

[1] J. Jiang, Z. Li, W. Li, P. Ranjan, X. Wei, X. Zhang, C. Zhang, *High Volt.* **2023**, *8*, 209.
[2] Z. Song, C. Liu, *Appl. Energy* **2022**, *322*, 119472.
[3] a) I. Mademlis, V. Mygdalis, N. Nikolaidis, M. Montagnuolo, F. Negro, A. Messina, I. Pitas, *IEEE Trans. Broadcast.* **2019**, *65*, 627; b) L. Shao, F. Nagata, H. Ochi, A. Otsuka, T. Ikeda, K. Watanabe, M. K. Habib, *Artif. Life Robot.* **2020**, *25*, 488.

[4] a) E. Straffelini, S. Cucchiaro, P. Tarolli, *Earth Surf. Process. Landforms* **2021**, *46*, 1926. b) H. Zhang, P. Shi, G. Crucil, B. Van Wesemael, Q. Limbourg, K. Van Oost, *Land Degrad. Dev.* **2021**, *32*, 4375.
[5] a) Y. Diez, S. Kentsch, M. Fukuda, M. L. L. Caceres, K. Moritake, M. Cabezas, *Remote Sens.* **2021**, *13*, 2837; b) I. M. McNicol, E. T. A. Mitchard, C. Aquino, A. Burt, H. Carstairs, C. Dassi, A. Modinga Dikongo, M. I. Disney, *J. Geophys Res. Biogeosci.* **2021**, *126*, e2021JG006586.
[6] a) H. Zhang, X. Li, *Trans. Emerg. Telecommun. Technol.* **2023**, *34*, e4737; b) M. Song, Z. Liang, Y. Huo, R. Liu, *Electron. Lett.* **2023**, *59*, e12979.
[7] a) S. Imai, E. Blasch, A. Galli, W. Zhu, F. Lee, C. A. Varela, *IEEE Aerosp. Electron. Syst. Mag.* **2017**, *32*, 4; b) E. Kakaletsis, C. Symeonidis, M. Tzelepi, I. Mademlis, A. Tefas, N. Nikolaidis, I. Pitas, *ACM Comput. Surv.* **2021**, *54*, 181.
[8] a) B. Fan, Y. Li, R. Zhang, Q. Fu, *Chin. J. Electron.* **2020**, *29*, 199; b) Z. Dennis, T. Holzer, *Syst. Eng* **2023**, *26*, 800.
[9] Y. Wan, T. Keviczky, *Int. J. Robust Nonlinear Control* **2019**, *29*, 5394.
[10] L. Sankaralingam, C. Ramprasadh, *Chin. J. Aeronaut.* **2020**, *33*, 749.
[11] M. A. Aleman, A. Gopalarathnam, K. Granlund, *J. Aircr.* **2022**, *59*, 1382.
[12] J. Valasek, J. Harris, S. Pruchnicki, M. Mccrink, J. Gregory, D. G. Sizoo, *J. Guid. Control Dyn.* **2020**, *43*, 1039.
[13] W. Koch, R. Mancuso, R. West, A. Bestavros, *TCPS* **2019**, *3*, 22.
[14] a) E. Balestrieri, P. Daponte, L. De Vito, F. Picariello, I. Tudosa, *Sensors* **2021**, *21*, 8253; b) D. Han, Q. Yang, R. Wang, *AMA J. Ethics* **2020**, *2020*, 540.
[15] W. Grodzki, A. Lukaszewicz, *Materwiss Werksttech* **2015**, *46*, 269.
[16] a) F. Bateman, H. Noura, M. Ouladsine, *IEEE Trans. Aerosp. Electron. Syst.* **2011**, *47*, 2119; b) L. M. Sanchez-Rivera, R. Lozano, A. Arias-Montano, *Drones* **2020**, *4*, 71.
[17] S. Y. Derakhshandeh, Z. Mobini, M. Mohammadi, M. Nikbakht, *IEEE Trans. Smart Grid.* **2019**, *10*, 4628.
[18] X. Wang, R. Liao, C. Shi, S. Wang, *Sensors* **2017**, *17*, 2444.
[19] Y. X. Guo, C. Lai, Z. B. Shao, K. L. Xu, T. Li, *Sensors* **2019**, *19*, 2210.
[20] a) M. R. Nabavi, S. N. Nihtianov, *IEEE Sens. J.* **2012**, *12*, 3346; b) S.-C. Wang, B.-R. Xie, S.-M. Huang, *Sensors* **2022**, *22*, 7444.
[21] Z. Dong, X. Sun, C. Chen, H. Yang, L. Yang, *Mech. Syst. Signal Process.* **2019**, *122*, 403.
[22] a) Z. L. Wang, *Adv. Energy Mater.* **2020**, *10*, 2000137; b) X. Ji, T. Zhao, X. Zhao, X. Lu, T. Li, *Adv. Mater. Technol.* **2020**, *5*, 1900921; c) C. Li, D. Liu, C. Xu, Z. Wang, S. Shu, Z. Sun, W. Tang, Z. L. Wang, *Nat. Commun.* **2021**, *12*, 2950.
[23] a) X. Cao, Y. Jie, N. Wang, Z. L. Wang, *Adv. Energy Mater.* **2016**, *6*, 1600665; b) Z. Xu, L. N. Y. Cao, C. Li, Y. Luo, E. Su, W. Wang, W. Tang, Z. Yao, Z. L. Wang, *Nat. Commun.* **2023**, *14*, 2792; c) E. Su, H. Li, J. Zhang, Z. Xu, B. Chen, L. N. Y. Cao, Z. L. Wang, *Adv. Funct. Mater.* **2023**, *33*, 2214934.
[24] a) X. He, Y. Zi, H. Guo, H. Zheng, Y. Xi, C. Wu, J. Wang, W. Zhang, C. Lu, Z. L. Wang, *Adv. Funct. Mater.* **2017**, *27*, 1604378; b) Y. Luo, P. Chen, L. N. Y. Cao, Z. Xu, Y. Wu, G. He, T. Jiang, Z. L. Wang, *Adv. Funct. Mater.* **2022**, *32*, 2205710.